International Journal of Hydrogen Energy 79 (2024) 186–198

Contents lists available at ScienceDirect

International Journal of Hydrogen Energy

journal homepage: www.elsevier.com/locate/he

$CuGaS_2$@NH_2-MIL-125(Ti) nanocomposite: Unveiling a promising catalyst for photocatalytic hydrogen generation

Anna Pancielejko [a,**], Hanna Głowienke [a], Magdalena Miodyńska [a], Anna Gołąbiewska [a], Tomasz Klimczuk [b], Mirosław Krawczyk [c], Krzysztof Matus [d], Adriana Zaleska-Medynska [a,*]

[a] Department of Environmental Technology, Faculty of Chemistry, University of Gdansk, 80-309, Gdansk, Poland
[b] Faculty of Applied Physics and Mathematics and Advanced Materials Centre, Gdansk University of Technology, 80-233, Gdansk, Poland
[c] Institute of Physical Chemistry, Polish Academy of Sciences, 01-224, Warsaw, Poland
[d] Faculty of Mechanical Engineering, Silesian University of Technology, 44-100, Gliwice, Poland

ARTICLE INFO

Handling Editor: Ramazan Solmaz

Keywords:
MOFs
NH_2-MIL-125(Ti)
$CuGaS_2$
Nanocomposite
H_2 generation
AQE

ABSTRACT

The development of efficient nanocomposites represents a promising strategy for enhancing the transfer and separation of photogenerated carriers within metal-organic frameworks (MOFs) for photocatalytic H_2 generation. In this study, we report, for the first time, the successful fabrication of a novel $CuGaS_2$@NH_2-MIL-125(Ti) nanocomposite in a two-step synthesis, consisting of octahedral NH_2-MIL-125(Ti) metal-organic frameworks interspersed with flat hexagonal plates of $CuGaS_2$. The $CuGaS_2$@NH_2-MIL-125(Ti) nanocomposite effectively mitigates the recombination rate of photogenerated electron-hole pairs. Notably, the most active $CuGaS_2$@NH_2-MIL-125(Ti) composite (containing 30 wt% $CuGaS_2$) achieves a remarkable hydrogen generation rate of 965.07 μmol/g_{cat}, surpassing the performance of NH_2-MIL-125(Ti) and $CuGaS_2$ by approximately 83 and 144 times, respectively. Additionally, the apparent quantum efficiency for the most active material at a wavelength of 380 nm is 9.07%. This study provides valuable insights into the design of efficient I-III-VI2 compound-MOF nanocomposites for H_2 generation applications.

1. Introduction

In the pursuit of sustainable production alternatives, the imperative for novel approaches like heterogeneous photocatalysis has become increasingly evident. Conventional methods frequently carry environmental impacts, necessitating innovative solutions. Heterogeneous photocatalysis, leveraging light-induced reactions on diverse catalytic surfaces, offers a promising approach for cleaner and more resource-efficient production. This cutting-edge pathway represents a crucial stride towards a sustainable industrial future, minimizing environmental impact while optimizing resource utilization.

Metal-organic frameworks (MOFs) have emerged as a compelling class of crystalline materials characterized by their intricate structures and diverse functionalities. Comprising metal nodes or clusters intricately coordinated with organic linkers, these porous materials form extended low- and three-dimensional networks [1,2]. Noteworthy for their exceptional properties, including high surface areas, tunable porosities, and versatile chemical functionalities, MOFs have become versatile platforms with applications from gas storage and separation to photocatalysis and drug delivery [3–7]. Particularly, the use of MOF as photocatalysts for hydrogen evolution is of great interest [8,9]. Rational design and the variation of building units can enhance the potential of MOFs for the H_2 evolution reaction [10,11]. Recently, numerous studies have described the improved light absorption capabilities of MOFs and facilitated the separation of photogenerated charges by modifying the structures of MOF materials or creating MOF composites and derived materials, contributing to overall increased performance [11–14].

Among well-known MOFs, NH_2-MIL-125(Ti), a porous titanium-based material, has garnered considerable attention from researchers owing to its efficient linker-to-metal charge transfer (LMCT) during visible light excitation [15]. Significantly, the MOF's LUMO-HOMO, representing the lowest unoccupied and highest occupied molecular orbitals, are specifically localized on the inorganic cluster and organic linker, respectively [16]. This spatial separation of light-induced charged species at the crystalline orbitals effectively impedes rapid electron−hole recombination, thereby promoting a conducive

* Corresponding author.
** Corresponding author.
E-mail addresses: anna.pancielejko@ug.edu.pl (A. Pancielejko), adriana.zaleska-medynska@ug.edu.pl (A. Zaleska-Medynska).

https://doi.org/10.1016/j.ijhydene.2024.06.416
Received 25 April 2024; Received in revised form 6 June 2024; Accepted 29 June 2024
Available online 5 July 2024

environment for photocatalytic reactions. Several studies have explored the application of NH_2-MIL-125(Ti) as photocatalysts for H_2 generation. For example, Kavuen et al. demonstrated that incorporating a single-site Co cocatalyst into the NH_2-MIL-125(Ti) structure significantly enhanced both the photoactivity and stability [15]. Additionally, this material benefits from improved light absorption, more efficient charge separation, and the formation of highly active proton reduction sites, contributing to their superior performance in hydrogen evolution reactions. Sun et al. proved that the introduction of Cu nanoparticles and mixed valence state of Cu^{2+}/Cu^{+} active site centers significantly enhanced the separation of photogenerated electron-hole pairs, thereby improving the visible-light response of MOF-based photocatalyst [17]. However, the stability of NH_2-MIL-125(Ti) remains suboptimal, and the limited oxidative capacity of the amino linker compromises the effectiveness of various sacrificial agents, such as methanol and triethanolamine, in promoting hydrogen evolution [18–21]. In response to these challenges, researchers have undertaken investigations into strategies for improving the photocatalytic properties of MOFs [22]. One promising approach involves the compositional integration of NH_2-MIL-125 (Ti) with other functional materials [15,20,23,24]. This concerted approach aims to exploit synergistic effects, mitigating the issue of rapid electron-hole recombination and potentially enhancing the overall photocatalytic performance of the composite materials.

Recently, there has been a notable interest in I-III-VI2 compounds, which are composed of one or more electropositive elements and at least one chalcogen ion (S^{2-}, Se^{2-}, or Te^{2-}) [25,26]. This increased attention is primarily attributed to their narrow band gap energy, abundance in the Earth, and environmentally benign characteristics. These photocatalysts are considered sustainable alternatives to toxic semiconductors for photocatalytic H_2 evolution and CO_2 photoconversion due to their negative conduction band (CB) potentials [25,27–30]. Among them, copper gallium sulfide ($CuGaS_2$) is a p-type low toxic semiconductor with a narrow band gap (~2.49 eV) and a high absorption coefficient [31]. There are some works on the application of $CuGaS_2$ for photocatalytic H_2 generation [32–35]. However, the photocatalytic performance of pristine $CuGaS_2$ in the hydrogen evolution reaction and CO_2 photoconversion is often limited by the mobility of photogenerated charge carriers, leading to rapid recombination before reaching material surfaces. To overcome these challenges, several approaches were employed: i) morphology and structure regulation [36,37], ii) element substitution or defect introduction [35,38], iii) incorporation of cocatalysts [31,34], and iv) construction of heterojunctions [35,39].

Some interesting works have explored the synergistic potential of I–III–VI2 ternary compounds and MOFs in diverse combinations, elucidating their applications as innovative photocatalysts. For example, Liu et al. described the fabrication process, inherent properties, and photocatalytic performance in the degradation of organic dyes for $CuInS_2$@ZIF-8 nanocomposites [40]. The authors realized that the pivotal factor governing the nucleation of ZIF-8 on the surface of $CuInS_2$ nanoparticles was attributed to the pyrrolidone rings within polyvinylpyrrolidone (PVP), thereby providing an enhanced affinity between $CuInS_2$ and Zn ions. The photocatalytic performance of $CuInS_2$@ZIF-8 nanocomposites under UV light was higher than that of pristine $CuInS_2$ and ZIF-8 due to a possible synergistic effect between those two composite components. Nevertheless, the composite exhibited lower photodegradation efficiency under simulated solar irradiation, even lower than pristine $CuInS_2$, due to the compact formation of ZIF-8 nanoparticles on the outer layer of $CuInS_2$@ZIF-8 hinders full penetration of visible light, limiting its absorption by the inner $CuInS_2$. Nguyen et al. synthesized the composite material by embedding $CuInS_2$ nanoplates into MIL-101(Cr) [41]. As revealed, the $CuInS_2$@MIL-101(Cr) nanocomposite demonstrated improved photocatalytic efficiency under visible light irradiation owing to its low bandgap energy. Evaluation for tetracycline photodegradation revealed an impressive degradation efficiency of 98.8% attributed to the decreased recombination of electrons and holes, along with the increase in the surface area of the nanocomposite. Pham et al. demonstrated a novel $AgInS_2$@MIL-101(Cr) heterostructure where MOF was synthesized from polyethylene terephthalate plastic waste [42]. The $AgInS_2$ nanoparticles were uniformly affixed to each lattice plane of the octahedral MIL-101(Cr) structure forming the composite with well-distribution of $AgInS_2$ nanoparticles into a porous MOF matrix. The authors demonstrated that the nanocomposite exhibited almost 100% efficiency of photocatalytic tetracycline degradation after 4 h of visible light irradiation. However, there are only a few studies on applying such composites for photocatalytic hydrogen generation. Liu et al. fabricated $ZnInS_2$@NH_2-MIL-125(Ti) nanocomposites with varying MOF content by dispersing $ZnInS_2$ nanosheets onto the surface of NH_2-MIL-125(Ti) [43]. The photocatalytic performance was examined in the context of H_2 evolution under visible light irradiation. The nanocomposite demonstrated a remarkable 6.5-fold increase in H_2 production rate compared to the corresponding pristine samples, attributed to a well-matched band structure and close contact between the two components. Jin et al. detailed the fabrication of a hierarchical Z-scheme junction between $ZnIn_2S_4$ and PCN-224 using the solvothermal method [44]. The combination with MOF enabled the unfolding of $ZnIn_2S_4$ microspheres, distributing nanosheets uniformly on the surface of the PCN-224 cube. The authors attribute the significantly improved photocatalytic efficiency for both H_2 evolution and the degradation of tetracycline hydrochloride to the effective suppression of photogenerated carrier recombination. Yao et al. engineered a $ZnIn_2S_4$/P-Ni-MOF-74 Z-scheme by integrating $ZnIn_2S_4$ sheets on rhombic P-Ni-MOF-74 derived from Ni-MOF-74 [45]. This heterostructure was crafted through the phosphorization treatment of Ni-MOF-74 and the hydrothermal synthesis of $ZnIn_2S_4$ flakes. The rhombic morphology of the heterostructure enhanced photoactive sites, expanded the light absorption spectrum, alleviated $ZnIn_2S_4$ agglomeration, mitigated photocorrosion issues, and accelerated the transfer and separation of photogenerated carriers. Consequently, the $ZnIn_2S_4$/P--Ni-MOF-74 heterojunction demonstrated improved photocatalytic hydrogen evolution under visible light irradiation. Meantime, Zhou et al. described the formation of $CdIn_2S_4$@NH_2-MIL-125 core-shell microsphere structure via hydrothermal technique. They revealed that constructing the heterojunction between the individual components effectively separates photogenerated electrons and holes, thereby significantly enhancing H_2 production [19]. Based on the above, it can be concluded that the combination of chalcogen and MOF in the nanocomposite facilitates the efficient separation of photogenerated electron-hole pairs. However, the number of works on the use of such kind of photocatalysts for H_2 production is limited to composites such as NH_2-MIL-125(Ti) combined with $ZnIn_2S_4$ [46], carbon dots [47] or Co_3O_4 [48]Moreover, the photocatalytic H_2 production capabilities of $CuGaS_2$ are not well understood.

In this context, we present a novel nanocomposite comprising amino-functionalized Ti-MOF (NH_2-MIL-125(Ti)) and I-III-VI2 compound, $CuGaS_2$, marking the first instance of such integration. Our research demonstrated that NH_2-MIL-125(Ti) is a matrix for embedding $CuGaS_2$ nanoplates, resulting in enhanced photocatalytic properties compared to the individual components. The synthesized materials showed outstanding photocatalytic performance for H_2 production under UV–Vis irradiation depending on the amount of $CuGaS_2$ used for the nanocomposite synthesis. We identified the optimal $CuGaS_2$ content to be 30 wt%, which resulted in the highest H_2 production efficiency of 965.1 $\mu mol/g_{cat}$. The calculated AQE of 9.07% at a wavelength of 380 nm further confirmed the high photocatalytic efficiency of the $CuGaS_2$@NH_2-MIL-125(Ti) nanocomposite. Besides, the durability of $CuGaS_2$@NH_2-MIL-125(Ti) was evaluated in a long-term stability test. Finally, we delved into a comprehensive discussion on the potential mechanism governing the photocatalytic reaction, offering valuable insights into the overall photocatalytic behavior of the developed nanocomposite.

2. Experimental section

Materials: The chemical reagents used in the study were as follows: N, N-Dimethylformamide (DMF, analytical pure), acetic acid (CH_3COOH, 99.5–99.9%), and acetonitrile (AcN, HPLC grade) sourced from POCH (Poland). Methanol (MeOH, analytical pure) was obtained from STANLAB (Poland). Other chemicals, including 1-dodecanethiol (DT, ≥98%), 1-octadecane (ODE, 90% technical grade), 2-aminoterephthalic acid (NH_2-BDC, 99%), and titanium (IV) isopropoxide (TPOT, 97%) were purchased from Merck (Germany). Copper(I) chloride (CuCl(I), 99.99% trace metal basis, extra pure), and gallium (III) chloride ($GaCl_3$, 99.99+% trace metal basis, anhydrous) were sourced from Acros Organics (Belgium). Triethanolamine (TEAO, analytical pure) was purchased from Chempur (Poland). Toluene, of analytical grade, was purchased from Eurochem BGD (Poland). Ethanol (99.8%) was purchased from POCH, Poland.

Synthesis of $CuGaS_2$ nanoplates: $CuGaS_2$ was synthesized according to the previously reported work [49]. In a 50 mL three-neck flask, 0.0494 g CuCl, 0.088 g $GaCl_3$, 1 mL DT, and 10 mL ODE were loaded. The flask was subsequently attached to a Schlenk line. The initial step involved subjecting the mixture to alternating cycles of vacuum and nitrogen for 30 min each, followed by heating to 90 °C, and an additional 30-min vacuuming. Subsequently, the flask was purged with nitrogen, heated to 270 °C for 40 min, and cooled naturally to room temperature. The resulting powder was collected by centrifugation and washed with toluene and ethanol. Finally, the purified $CuGaS_2$ powder was dried overnight.

Synthesis of CGS@MIL(Ti) nanoparticles: NH_2-BDC (0.543 g) was combined with a mixture comprising DMF (18 mL), CH_3COOH (2 mL), and MeOH (2 mL), stirring at room temperature for 10 min. Following this, a sustainable quantity of $CuGaS_2$ (CGS) powder (ranging from 10 to 60 wt%) was introduced, and TPOT (0.6 mL) was added, continuing the stirring for an additional 15 min. The resultant solution was then transferred into a Teflon-lined stainless-steel autoclave (50 mL) and maintained at 150 °C for 24 h. After cooling to room temperature, the suspension was centrifugated and washed three times with DMF and three times with MeOH. The obtained powder was activated under vacuum at 200 °C. The pristine NH_2-MIL-125(Ti) was prepared using a comparable procedure, excluding the $CuGaS_2$ addition. The procedure of the nanocomposite synthesis and photocatalytic application is covered by a patent application (No. P.448194).

Characterization: Room temperature X-ray powder diffraction (pXRD) analysis was performed using a Bruker D2 Phaser diffractometer, which featured a CuKα radiation source (λ = 1.5404 Å) and an XE-T detector. The sample powder was evenly distributed on a low-background silicon holder, and the resulting XRD patterns were analyzed using Bruker Topas software. The physical structure, dimensions, and morphology of particles were examined using the JEOL JSM-7610F scanning electron microscope (SEM) operating at 15 kV within a high vacuum environment. For detailed measurements, the Tecnai F20 X-Twin microscope from FEI, coupled with an EDAX spectrometer, was utilized in the transmission electron microscope (TEM) and energy-dispersive X-ray spectrometer (TEM-EDX) modes. The PHI 5000 VersaProbe (ULVAC-PHI) spectrometer was employed for X-ray photoelectron spectroscopic (XPS) analysis. It used monochromatic Al Kα radiation (hν = 1486.6 eV) generated by an X-ray source operating at 100 μm spot size, 25 W, and 15 kV. High-resolution (HR) XPS spectra were gathered using a hemispherical analyzer set at a pass energy of 117.4 and an energy step size of 0.1 eV. The incident X-ray beam struck the sample surface at a 45° angle relative to the surface normal, while the analyzer axis was positioned at 45° as well. Data analysis was conducted using CasaXPS software, involving deconvolution of HR XPS spectra employing a Shirley background and Gaussian peak shape with 30% Lorentzian character. The surface area, pore volume, and pore size characteristics of the acquired specimens were assessed utilizing a sorption analyzer, the 3P Instrument Micro 200, following the principles established by the BET (Brunauer-Emmett-Teller) method. To ensure the removal of any residual solvents, the sample underwent a degassing process at a temperature of 200 °C for 5 h before analysis. UV–visible spectra were acquired using the Thermo Scientific Evolution 220 UV–visible spectrophotometer within the wavelength range of 200–800 nm. Photoluminescence spectroscopy measurements were conducted at room temperature using an LS-50B photoluminescence spectrometer by Perkin Elmer Ltd. For excitation, a Xenon lamp was utilized, while an R928 photomultiplier facilitated detection. Spectra were recorded from 300 to 800 nm, with the excitation wavelength set at 330 nm and directed onto the sample surface at a 90° angle.

Photoactivity test: A 25 mg sample was dispersed in a solution composed of AcN (18 mL), TEOA (2 mL), and H_2O (300 μL). The mixture was agitated at 500 rpm within a quartz-sealed reactor maintained at a constant temperature of 10 °C. To establish adsorption-desorption equilibrium, the headspace above the suspension underwent a 30-min nitrogen purge before initiating irradiation. After obtaining a reference sample, the suspension was subjected to UV–Vis light using a 1000 W Xenon lamp (Oriel 66021). Hourly samples were withdrawn to measure the concentration of evolved H_2, and gas chromatography (TRACE 1300, Thermo Scientific) equipped with a HayeSep Q (80/100) column and a thermal conductivity detector (TCD) with nitrogen as the carrier gas was employed for analysis. Consistency was ensured by examining multiple sample replicates. The estimation of evolved H_2 was determined based on the calibration curve according to the procedure described by our groups previously [50].

The electrolytes were examined both before and after the process of H_2 generation. This examination was carried out using a headspace gas chromatograph mass spectrometer (GC-2010 Plus and GCMS-QP2010 SE, manufactured by Shimadzu), which was equipped with a SH-Stabliwax column. Helium was used as the carrier gas, with 200 μL of the sample injected. Sample preparation involved agitation at 80 °C with continuous mixing for 10 min. The column temperature was maintained at 30 °C, with a purge flow rate of 3.0 mL per minute. The ion source temperature was set to 200 °C, and mass detection was conducted across the range of m/z 2 to 200.

Action spectra measurement: An 8.75 mg sample was placed in a quartz-sealed reactor containing 7 mL of solution of AcN/TEAO/H_2O solution. The mixture was agitated at 500 rpm and maintained at a constant temperature of 18 °C. To establish adsorption-desorption equilibrium, the headspace above the suspension underwent a 15-min nitrogen purge before initiating irradiation. After obtaining a reference sample, the suspension was irradiated using wavelengths of 380, 400, 420, and 440 nm. Irradiation intensity was measured with an optical meter (Thor Labs S130VC) for individual wavelength each. Notably, no hydrogen was generated under these conditions when the sacrificial agent solution was irradiated. The gaseous sample taken after 4 h of irradiation was withdrawn to measure the concentration of evolved H_2 (the procedure of the analysis is the same as the above described). Multiple sample replicates were examined for consistency.

The apparent quantum efficiency (AQE) as a function of wavelength was determined by calculating the ratio of the rate of hydrogen generation to the incident photons flux. This calculation assumed the reaction stoichiometry, requiring two photons for the process, and commenced from Eq. (1).

$$AQE = \frac{2 \bullet number\ of\ generated\ H_2\ molecules}{number\ of\ incident\ photons} \quad \text{Eg. (1)}$$

3. Results and discussion

To study the combination of $CuGaS_2$ and NH_2-MIL-125(Ti) into $CuGaS_2$@NH_2-MIL-125(Ti) (CGS@MIL(Ti)) nanocomposite on

Table 1
Sample label, $CuGaS_2$ content, surface properties, and photocatalytic performance of the obtained samples.

Sample label	$CuGaS_2$ amount (wt.%)	BET surface area (m^2/g)	Pore volume (cm^3/g)	Pore size (nm)	H_2 production rate ($\mu mol/(h \cdot g_{cat})$)
$CuGaS_2$	–	31	0.06	8.40	1.68
NH_2-MIL-125(Ti)	–	1280	0.65	2.03	2.92
CGS-10@MIL(Ti)	10	1195	0.61	2.03	29.67
CGS-20@MIL(Ti)	20	1065	0.55	2.08	38.22
CGS-30@MIL(Ti)	30	980	0.46	1.89	241.27
CGS-40@MIL(Ti)	40	908	0.49	2.17	142.80
CGS60@MIL(Ti)	60	552	0.33	2.52	4.44

morphology, structure, optical and photocatalytic properties, we prepared a series of photocatalysts with varied $CuGaS_2$ content. The sample label, $CuGaS_2$ content, surface properties, and photocatalytic efficiency of the as-prepared materials are summarized in Table 1.

3.1. Structure and morphology

Fig. 1 shows the XRD patterns of the pristine NH_2-MIL-125(Ti), $CuGaS_2$, and $CuGaS_2$@NH_2-MIL-125(Ti) (CGS@MIL(Ti)) nanocomposites with different amounts of $CuGaS_2$. The red and black vertical bars represent the expected Bragg positions for $CuGaS_2$ (wurtzite crystal structure) and NH_2-MIL-125(Ti), respectively. The powder diffraction pattern of the latter compound was refined by the LeBail method using a tetragonal I4/mmm structure. The lattice parameters obtained are a = 18.680 (1) Å and c = 18.149 (1) [51]. Fig. S1 presents room-temperature experimental and theoretical powder XRD patterns for the NH_2-MIL-125 (Ti). The XRD pattern of NH_2-MIL-125(Ti) revealed characteristic diffraction peaks compatible with literature data, indicating that the sample has been successfully prepared [52,53]. In the case of XRD analysis of CGS@MIL(Ti) nanocomposites, the diffraction peaks of NH_2-MIL-125(Ti) are distinct. On the other hand, reflection peaks of $CuGaS_2$ in CGS@MIL(Ti) nanocomposites were observed only for the higher content of $CuGaS_2$ in nanocomposites (CGS-40@MIL(Ti) and CGS-60@MIL(Ti)).

The structural characteristics of $CuGaS_2$, NH_2-MIL-125(Ti), and their composite materials were investigated through scanning electron microscopy (SEM) and transmission electron microscopy (TEM) with additional elemental mapping. The structure of $CuGaS_2$ resembles flat hexagonal plates, with sizes of particle edges ranging from approx. 50 nm to almost 400 nm, but most particles range from 50 to 175 nm (Fig. 2a and S2a). Pristine NH_2-MIL-125(Ti) showed mainly an octahedron shape with particle edge dimensions from approx. 250 to 475 nm (Fig. 2b and S2b). The CGS@MIL(Ti) samples reveal a combination of both structures. SEM and STEM images of composites depict the octahedra of NH_2-MIL-125(Ti) metal-organic frameworks with flat hexagonal plates of $CuGaS_2$ between them (Fig. 2c and d, Fig. S3, and Fig. S4). HRTEM analysis confirmed the presence of $CuGaS_2$ in the CGS-30@MIL(Ti) nanocomposite, with a lattice spacing of 0.31 nm observed between two consecutive fringes (Fig. 2f). Elemental mapping study for CGS-30@MIL(Ti), CGS-10@MIL(Ti), and CGS-60@MIL(Ti) (Fig. 2 and Fig. S5, respectively) confirmed the simultaneous presence of $CuGaS_2$ and NH_2-MIL-125(Ti) in the composite. For the CGS-30@MIL(Ti) sample, an additional EDX analysis was performed (Fig. S6). The results confirmed the presence of Cu, Ga, S, O, Ti, and C, indicating a good distribution of individual components in the composite.

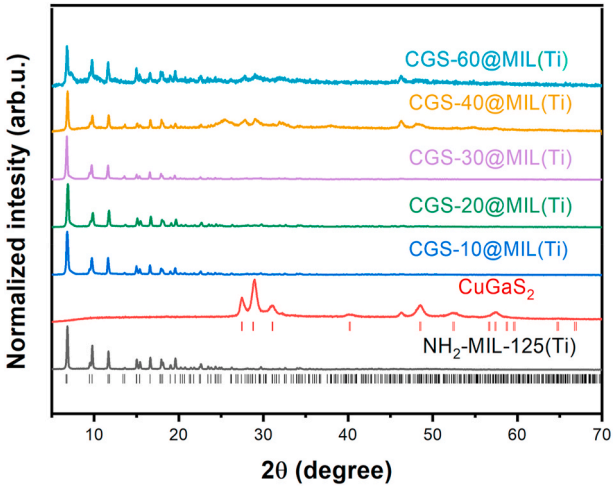

Fig. 1. XRD patterns of pristine NH_2-MIL-125(Ti), $CuGaS_2$, and CGS@MIL(Ti) nanocomposites.

Table 2 shows the surface elemental composition (in at.%) of NH_2-MIL-125(Ti), $CuGaS_2$, and CGS-30@MIL(Ti) samples evaluated by XPS. We noticed that the surface of both $CuGaS_2$ and CGS-30@MIL(Ti) samples reveals a relatively large content of carbon in the range of 28.7–35.3 at.%. The largest atomic concentrations of Cu (11.8 at.%) and S (37.6 at.%) are found for the $CuGaS_2$ sample. For the CGS-30@MIL(Ti) sample, both concentrations are significantly smaller, i.e. 0.7 at.% and 8.2 at.%, respectively. In addition, CGS-30@MIL(Ti) had the largest surface content of N atoms (19.2 at.%). As can be seen from Table 2, the surface concentration of Ti on NH_2-MIL-125(Ti) was found to be about 2 times larger than that evaluated for CGS-30@MIL.

Fig. S7 shows the high-resolution (HR) XPS spectra of Ti 2p, O 1s, N 1s, and C 1s with chemical characteristics, recorded from the surface of NH_2-MIL-125(Ti). The Ti 2p spectrum (Fig. 7a) is composed of Ti $2p_{3/2}$ (binding energy, BE of 459.0 eV) and Ti $2p_{1/2}$ (BE of 464.7 eV) signals characteristic of Ti^{4+} cations in stoichiometric TiO_2 [54,55]. Fig. S7b shows the O 1s spectrum, revealing only two oxygen peaks. The first peak located at BE of 530.3 eV is allocated to O^{2-} ions, and the second peak at BE of 531.9 eV is associated with oxygen atoms in surface –OH, C-O-C, and/or –COOH groups [54–56]. The N 1s spectrum of NH_2-MIL-125(Ti) (Fig. S7c) reveals three nitrogen peaks. The main peak (BE of 399.6 eV) can be attributed to nitrogen in C-NH-C and/or H-N-H surface bonds [55,56]. The nitrogen peak at BE of 401.0 eV is related to C-NH_3, N-N, and/or N_2H^+ surface species. The third peak at the largest BE = 402.8 eV is probably assigned to pyridinic nitrogen (pyri-N) [56]. Deconvolution of the C 1s spectrum recorded from NH_2-MIL-125(Ti) (Fig. S7d) reveals three chemical states of carbon. The first state (BE = 284.8 eV) is attributed to C atoms in C-C and/or C-H bonds. The second state at BE of 286.3 eV can be associated with C-O(H) and/or C-N bonds on the surface while the third carbon peak (BE of 288.8 eV) is assigned to O=C-OH species.

Figs. 3 and 4 present the HR XPS spectra of Ti 2p, O 1s, Cu 2p, Ga 2p, N 1s S 2p, and C 1s for the samples labeled $CuGaS_2$ and CGS-30@MIL (Ti), respectively. Except for the intensity, the Ti 2p spectrum recorded on CGS-30@MIL(Ti) (Fig. 4a) is similar to that recorded for NH_2-MIL-125(Ti). The O 1s spectrum of $CuGaS_2$ (Fig. 3a) contains two oxygen signals located at BE of 532.0 eV and 533.0 eV. The first signal can be attributed to oxygen in –OH, C-O-C, S-O, and/or Ga^{3+}-O bonds while the second wide signal is assigned to H_2O species. In contrast, there is only one oxygen peak in the O 1s spectrum of CGS-30@MIL(Ti) (Fig. 4b). The oxygen contribution at BE = 531.7 eV can be associated with oxygen in –OH, C-O-C, C=O, S-O, Ga^{3+}-O, and/or Ti^{4+}-O surface bonds. The Cu 2p spectrum of $CuGaS_2$ (Fig. 3b) reveals two Cu $2p_{3/2}$ and

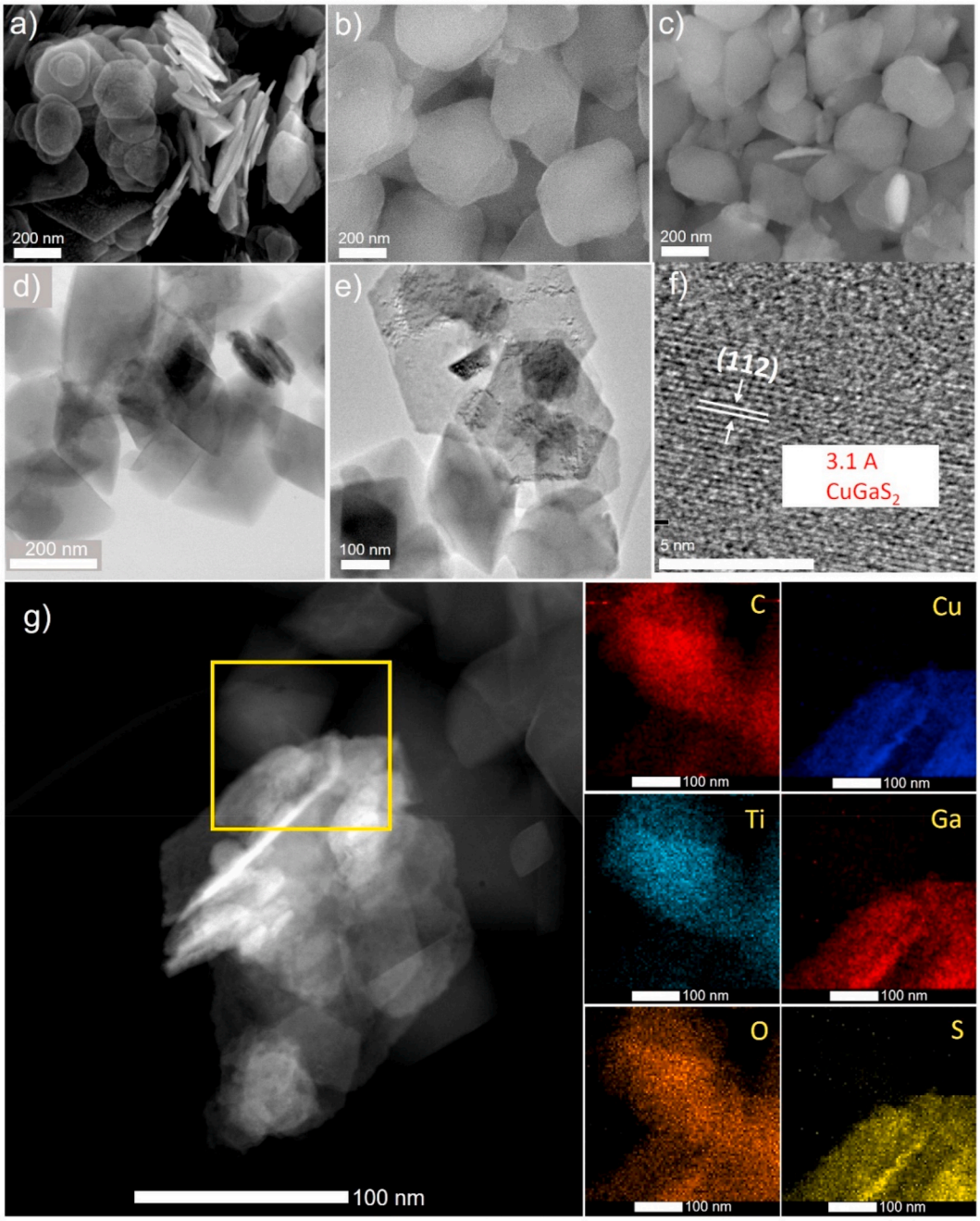

Fig. 2. SEM images of a) $CuGaS_2$, b) NH_2-MIL-125(Ti), c) CGS-30@MIL(Ti), d) STEM, e) TEM, and f) HRTEM images, and g) elemental mapping of CGS-30@MIL(Ti).

Table 2
Surface elemental composition (in at.%) of NH_2-MIL-125(Ti), $CuGaS_2$, and the CGS-30@MIL(Ti) composite evaluated by XPS.

Sample	%at. (in total)								
	C	Ti	O	N	Cu	Ga	S	Na	Cl
NH_2-MIL-125(Ti)	56.2	7.2	28.4	6.8	–	–	–	1.4	–
$CuGaS_2$	28.7	–	9.0	–	11.8	9.4	37.6	–	3.5
CGS-30@MIL(Ti)	35.3	3.9	26.1	19.2	0.7	6.4	8.2	–	–

Cu $2p_{1/2}$ signals of high intensity. Both the Cu $2p_{3/2}$ signal located at 932.5 eV and the principal Cu LMM Auger line (not shown here) at a kinetic energy (KE) of 916.5 eV confirm the presence of the Cu^+ oxidation state [57]. The Cu 2p spectrum recorded from CGS-30@MIL (Ti) (Fig. 4c) is very similar but its intensity is considerably smaller. We identify the Cu $2p_{3/2}$ signal at BE of 933.2 eV characteristic of the mixed Cu^{2+}/Cu^+ oxidation states. The presence of Cu^+ can data also be confirmed by the Cu LMM kinetic energy from this sample. For the $CuGaS_2$ sample, the Ga 2p spectrum (Fig. 3c) contains the Ga $2p_{3/2}$ signal (BE of 1118.2 eV) characteristic for the Ga^{3+} species [54,55].

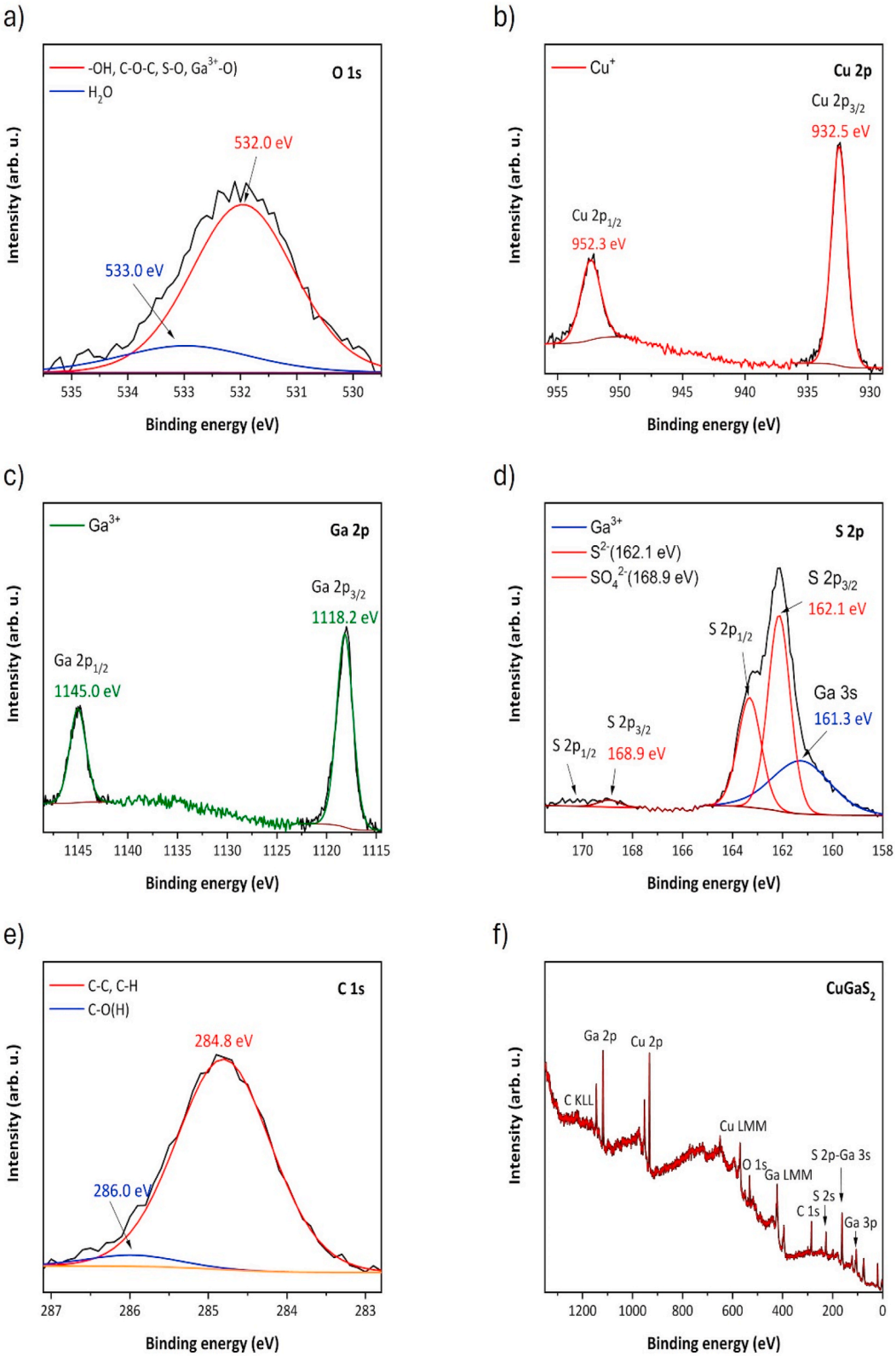

Fig. 3. High-resolution (HR) XPS spectra of O 1s, Cu 2p, Ga 2p, S 2p, and C 1s with chemical characteristics and survey spectrum of the $CuGaS_2$ sample.

Deconvolution of the same spectrum of CGS-30@MIL(Ti) (Fig. 4d) reveals the two Ga $2p_{3/2}$ peaks at BEs of 1118.3 eV and 1119.9 eV, which can be assigned to α-Ga^{3+} and β- Ga^{3+} species. The N 1s spectrum of CGS-30@MIL(Ti) (Fig. 4e) coincides with the Ga LMM Auger signal. After deconvolution, we identified the N 1s spectral features characteristic of C-NH-C/H-N-H (BE = 399.2 eV) and CH_6N^+ (BE = 402.4 eV) species. The S 2p spectrum of $CuGaS_2$ (Fig. 3d) overlaps with the Ga 3s signal, but after deconvolution, it displays two contributions to the S 2p region: one associated with the S^{2-} species (S $2p_{3/2}$ BE = 162.1 eV), and the second one associated with a sulfate (S $2p_{3/2}$ BE = 168.9 eV)

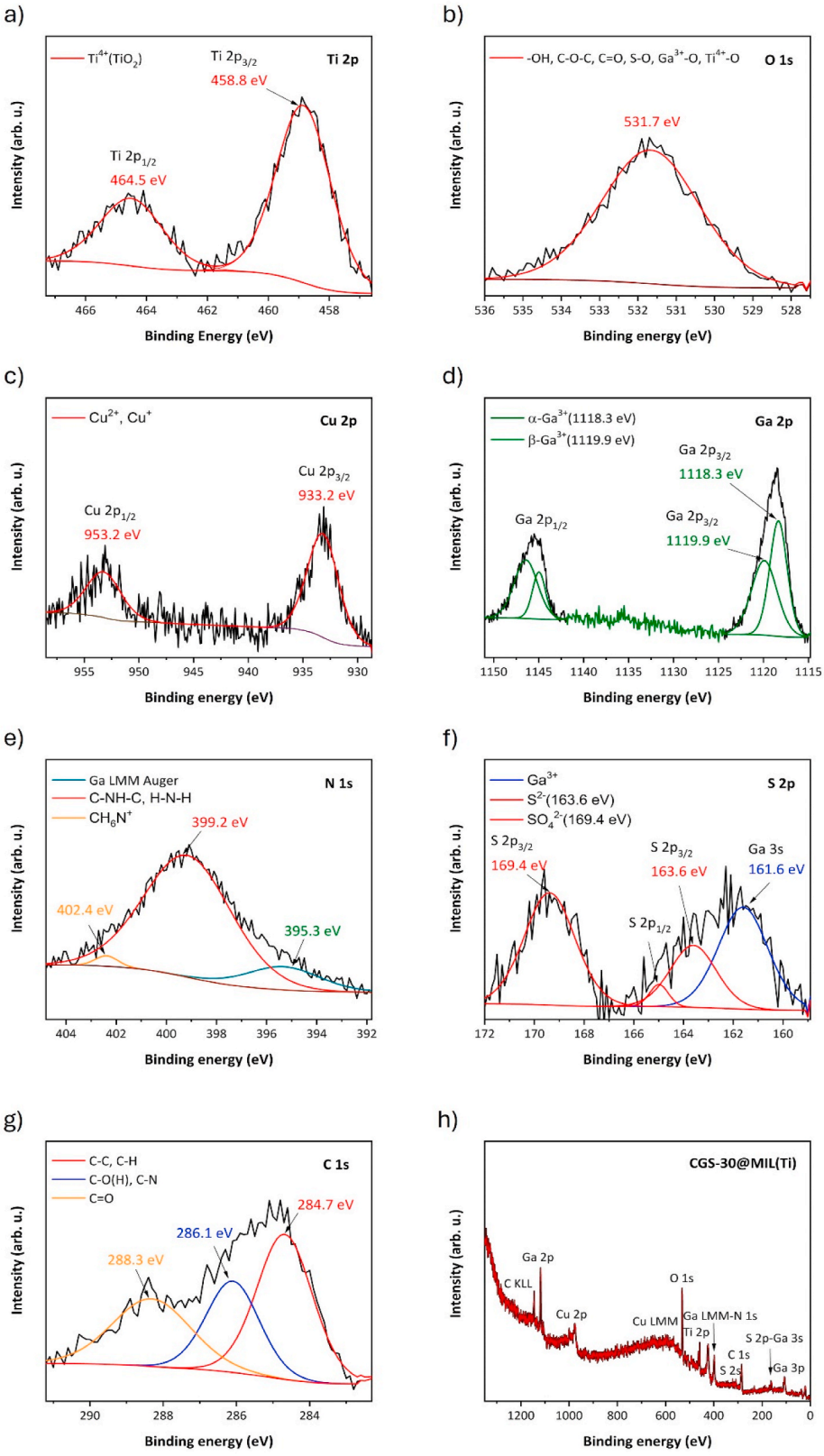

Fig. 4. High-resolution (HR) XPS spectra of Ti 2p, O 1s, Cu 2p, Ga 2p, N 1s, S 2p, and C 1s with chemical characteristics and survey spectrum of the CGS-30@MIL (Ti) composite.

[54,55,58]. The S 2p spectrum recorded from CGS-30@MIL(Ti) (Fig. 4f) seems to be similar to that of $CuGaS_2$ except for the smaller intensity and positioning of the deconvoluted peaks. The C 1s spectrum of $CuGaS_2$ (Fig. 3e) reveals two chemical states of C atoms. The first state (BE of 284.8 eV) is attributed to C-C and/or C-H bonds while the second state (BE of 286.0 eV) can be associated with C-O(H) bonds on the surface. For the CGS-30@MIL(Ti) surface, the C 1s spectrum (Fig. 4g) confirms the presence of C-C/C-H (BE = 284.7 eV), C-O(H)/C-N (BE = 286.1 eV) and C=O (BE = 288.3 eV) bonds.

The specimens comprising pristine NH_2-MIL-125(Ti) and MOF treated with varying quantities of $CuGaS_2$ nanocrystals were subjected to surface property evaluations, focusing on specific surface area, pore size, and pore volume. The findings are summarized in Table 1. NH_2-MIL-125(Ti) belongs to the category of microporous materials, demonstrating a significant BET surface area (1280 m^2/g) [59]. However, the surface modification of NH_2-MIL-125(Ti) with differing quantities of $CuGaS_2$, characterized by a low BET area (31 m^2/g), results in a linear decrease in the specific surface area of the composites compared to the pristine MOF. This indicates a clear correlation between the increasing contribution of $CuGaS_2$ with a smooth surface in the composite CGS@MIL(Ti) mass. The smooth surface of $CuGaS_2$ not only exhibits a small surface area but also an extremely low pore volume (0.064 cm^2/g) compared to NH_2-MIL-125(Ti) (0.65 cm^2/g). Naturally, a reduction in pore volume in the composites was observed with an increase in the proportion of $CuGaS_2$ in the composite. Furthermore, N_2 adsorption-desorption isotherms were conducted for all samples, as illustrated in Fig. 5. Consistently, the type I isotherm shape was observed for pristine NH_2-MIL-125(Ti) and CGS@MIL(Ti) composites with characteristic hysteresis loops (Fig. 5a). These isotherms exhibit nearly parallel behavior across a broad relative pressure range of 0.05–1. However, due to the minimal N_2 adsorption by $CuGaS_2$, the isotherm for $CuGaS_2$ was expanded in Fig. 5b, revealing a type III shape with a characteristic hysteresis loop in the relative pressure range ~0.6–1.0.

3.2. Optical properties

Fig. 6a displays the UV–visible spectra of CGS@MIL(Ti) samples alongside pristine NH_2-MIL-125(Ti) and $CuGaS_2$. In the CGS@MIL(Ti) series, all samples exhibit two absorption peaks located approximately at 275 nm and 390 nm. These peaks can be ascribed to the presence of Ti-O oxo-clusters and ligand-based absorption, respectively, within the NH_2-MIL-125(Ti) metal-organic framework [59–61]. The pristine $CuGaS_2$ sample also shows two absorption bands with a maximum of around 275 nm and 400 nm, but the absorption band extended further toward infrared light, suggesting a strong absorption of the $CuGaS_2$ in the visible range. The optical bandgap determined by the Kubelka-Munka transformation of as-synthesized NH_2-MIL-125(Ti) and $CuGaS_2$ were 2.64 and 2.06 eV, respectively (Fig. S8). It is speculated that due to the copper-rich $CuGaS_2$ sample, its bandgap was smaller than the literature data [49,62,63]. Interestingly, the introduction of $CuGaS_2$ to the synthesis of NH_2-MIL-125(Ti) allows obtaining structures with absorption spectra also increasing towards the infrared - we observe a significant broadening of the absorption band in the range from approximately 500 nm–800 nm compared to pristine NH_2-MIL-125(Ti). Thus, we can conclude that the CGS@MIL(Ti) series samples suggest significantly higher photocatalytic activity in visible light than pristine NH_2-MIL-125(Ti).

Utilizing the photoluminescence (PL) technique provides insights into the characteristics of emitted radiation resulting from the recombination effects of photogenerated electron-hole pairs. Fig. 6b illustrates the emission spectra of the samples, showing distinct photoluminescence spectra depending on the proportion of $CuGaS_2$ in each sample. The intensity of the PL peak is directly linked to the recombination rate, with a higher peak value indicating a higher recombination rate [64]. According to the presented findings, the incorporation of $CuGaS_2$ with NH_2-MIL-125(Ti) reduces the recombination effects. Specifically, the CGS-30@MIL(Ti) sample exhibits the lowest intensity of photoluminescence, indicating the slowest recombination of electron-hole pairs among the tested samples, thereby suggesting its high photocatalytic performance.

3.3. Photocatalytic performance

The prepared samples were examined for their photocatalytic effectiveness under both UV–Vis and Vis (>420 nm) irradiation hydrogen production employing triethanolamine (TEAO) as a sacrificial agent. Fig. 7 illustrates that when pristine NH_2-MIL-125(Ti) alone is used as the photocatalyst, the hydrogen production is approximately 11.7 $\mu mol/g_{cat}$, indicating that NH_2-MIL-125(Ti) alone exhibits limited efficiency as a photocatalyst for hydrogen production, consistent with the literate data summarized in Table S1 [15,17,19,21,65]. The situation deteriorated further when pristine $CuGaS_2$ was used, as only a negligible amount of hydrogen was detected. A similar lack of photoactivity was observed by Caudillo-Flores et al. and others, as presented in Table S2 [34,35]. After coupling $CuGaS_2$ with NH_2-MIL-125(Ti), a significant enhancement in the photoactivity is observed. The production rate of H_2 of the resulting nanocomposites exhibits a substantial increase with increasing $CuGaS_2$ amount, achieving the maximum of 241.3 $\mu mol\ h^{-1}$

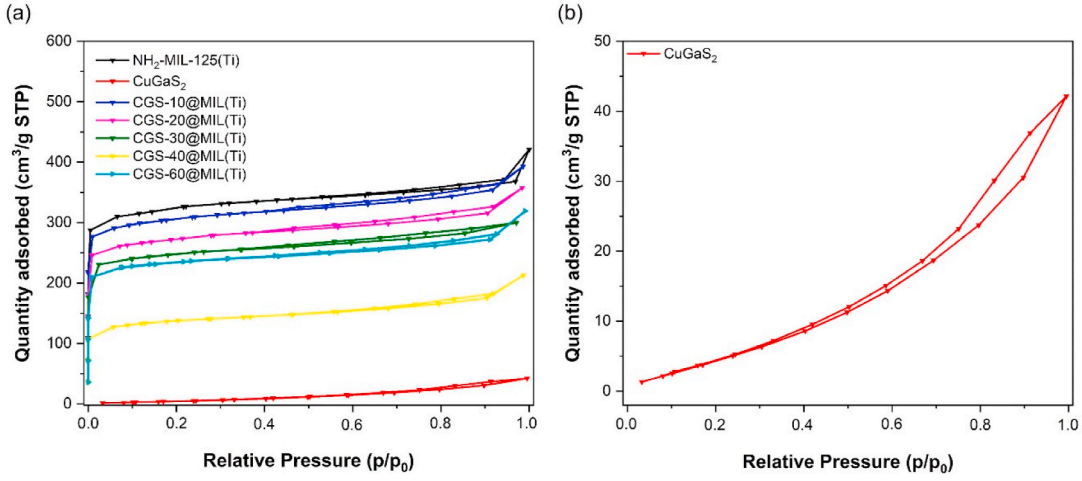

Fig. 5. a) N_2 adsorption-desorption isotherms for pristine NH_2-MIL-125(Ti), $CuGaS_2$ and their composites; b) expanded N_2 adsorption-desorption isotherm of $CuGaS_2$.

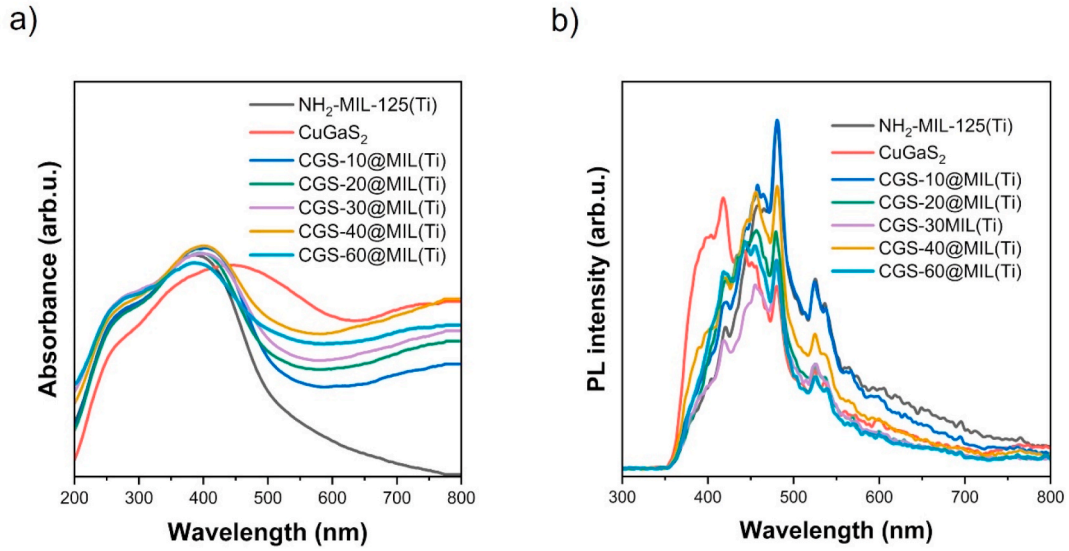

Fig. 6. a) UV–Vis absorption spectra, and b) PL spectra (λ_{ex} = 330 nm) of the prepared samples.

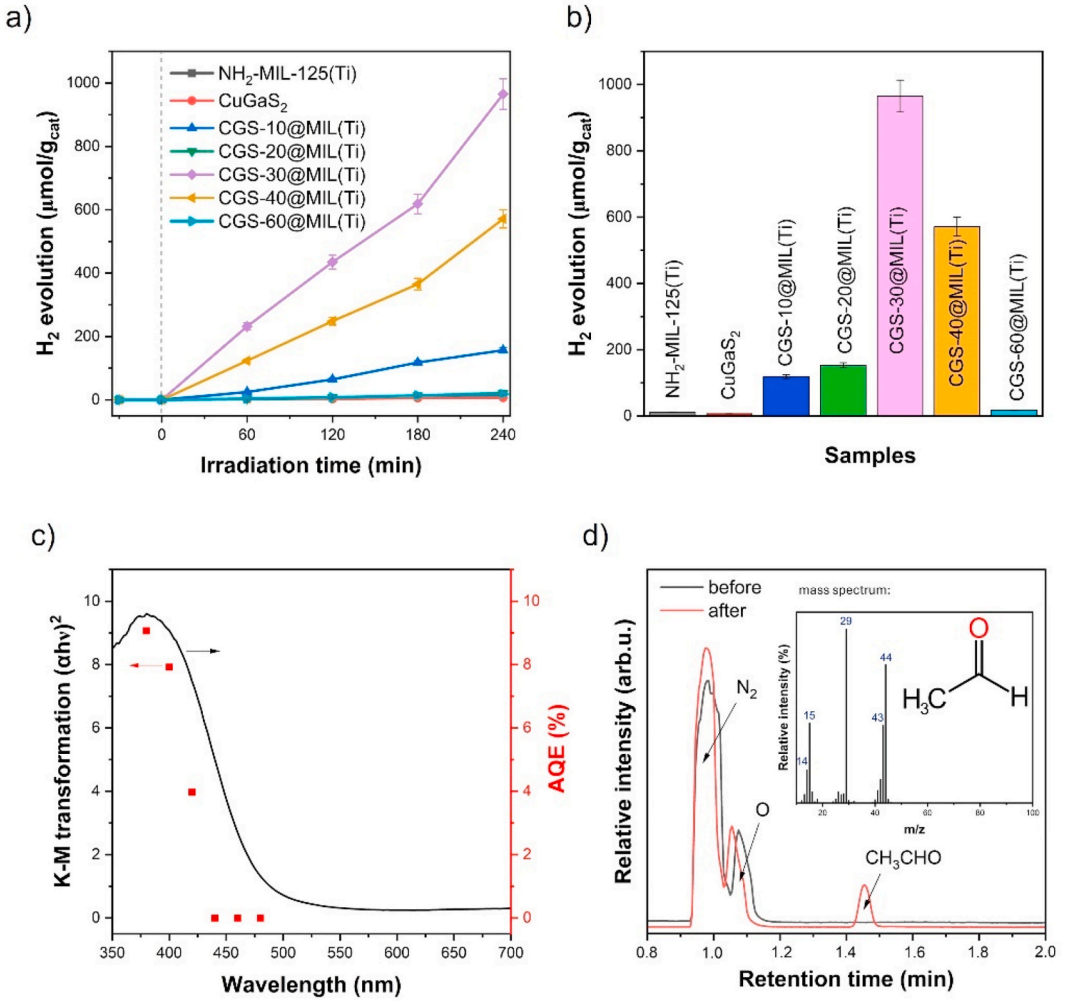

Fig. 7. a). Rate of H_2 generation under UV–Vis irradiation, b) the efficiency of H_2 generation after 4 h of UV–Vis irradiation, c) AS measurement for the CGS-30@MIL (Ti) sample, and d) headspace GC/MS spectra of the electrolyte (AcN/TEAO, 18/2 v/v) before and after 4 h of the UV–Vis irradiation during H_2 generation reaction in the presence of CGS-30@MIL(Ti) sample.

g^{-1} at a concentration of 30 wt%, which is about 83 and 144 times higher than pristine NH_2-MIL-125(Ti) and $CuGaS_2$, respectively. However, a further increase in the amount of $CuGaS_2$ leads to a decline in photocatalytic H_2 production. This observation can be attributed to the following factors: (i) the increased content of $CuGaS_2$, being a non-active phase, leads to a decrease in the photoactivity of the nanocomposites, and (ii) an excess $CuGaS_2$ can transform into a recombination center of photoinduced charges (as confirmed by the PL measurement in Fig. 4b), resulting in the reduction of activity. Consequently, an optimal ratio of $CuGaS_2$ to NH_2-MIL-125(Ti) amount is the key to achieving the maximum H_2 evolution of CGS@MIL(Ti) nanocomposites. The measurements conducted under visible light illumination showed negligible activity for both the individual components and the nanocomposites. Compared with the literature data, it can be assumed that, up to now, the most frequently used electrolyte for the chalcogenide-MOF compositions were composed of Na_2S and Na_2SO_3 aqueous solution [19,65]. However, we suggest that employing TEAO as a sacrificial agent is a better solution because it is less likely to cause photocorrosion or structural degradation of NH_2-MIL-125(Ti), does not generate by-products (e.g., Na_2S can produce sulfur or polysulfide by-products), and thus the reaction mechanism is more straightforward compared to complex interaction and side reactions that can occur with Na_2S and Na_2SO_3.

To understand the mechanism behind photocatalytic H_2 evolution, we carried out action spectra (AS) analysis using the most active sample, CGS-30@MIL(Ti). The apparent quantum efficiency (AQE) was calculated as a function of the irradiated light (380, 400, 420, and 440 nm) and the results are shown in Fig. 7c and Table S3. The highest AQE of 9.07% was found for the measurement conducted at 380 nm. Following exposure to wavelengths of 400 and 420 nm, the AQE values were determined to be 7.92, and 3.97%, respectively. Notably, for higher wavelengths (beyond 440 nm), AQE dropped to 0%. As shown in Fig. 7c, the results of AQE and absorption spectra show a similar trend. It is suggested if the efficiency of photoabsorption is higher, the efficiency of electron-hole utilization is lower, and the AQE could be shifted to the lower wavelengths.

The durability of the photocatalysts was conducted in a prolonged 24-h UV–Vis irradiation-driven H_2 evolution under similar experimental conditions as employed for H_2 evolution with CGS-30@MIL(Ti). The results, depicted in Fig. 8a, reveal a continued increase of H_2 evolution up to 2195 μmol/g_{cat} with the extension of the irradiation process. However, analysis of the XRD data presented in Fig. 8b revealed a lack of stability in the nanocomposite under the reaction conditions, particularly concerning the NH_2-MIL-125(Ti) component, while patterns corresponding to $CuGaS_2$ remained prominent.

Going into an in-depth understanding of the material fate, we investigated the structural changes of pristine $CuGaS_2$ and NH_2-MIL-125 (Ti) after the photocatalytic process. Remarkably, both individual components exhibited stable performance after 4 h of UV–Vis irradiation (Figs. S9a and b). However, their structural stability diminished when combined into a nanocomposite, especially in the long-term photoprocess. We hypothesized that NH_2-MIL-125(Ti) may not be compatible with $CuGaS_2$ under these specific conditions, as evidenced by XRD analysis showing prominent $CuGaS_2$ phases and minimal NH_2-MIL-125 (Ti) patterns. Moreover, the composition of the electrolyte, notably the presence of $CuGaS_2$, could influence the solution's pH. NH_2-MIL-125(Ti) might be sensitive to pH changes, leading to its degradation or instability. It is known that NH_2-MIL-125(Ti) can decompose in alkaline conditions due to various factors, including hydrolysis of metal-ligand bonds, protonation of amino functional groups, and site reactions such as the interaction of hydroxide ions (OH^-) with metal ions in the framework, resulting in the dissolution or precipitation of metal hydroxides or oxides (e.g., TiO_2 anatase phase, Fig. 8b). However, the detection of variations in the pH of different electrolyte types (including pristine electrolyte, electrolyte post-photocatalytic process with NH_2-MIL-125(Ti), $CuGaS_2$, and CGS-30@MIL(Ti)) was scarcely discernible. The final hypothesis pertains directly to the photoprocess mechanism, specifically the photogenerated electrons with the highest reducing potential within the conduction band (CB) of $CuGaS_2$. These electrons, owing to their elevated potential, are posited to potentially instigate the degradation of the MOF present within the composite.

The valence band (VB) of $CuGaS_2$ and NH_2-MIL-125(Ti) has been estimated from XPS data by linear extrapolation of the low binding energy edge of the VB spectrum. As shown in Fig. S10, the VB of $CuGaS_2$ and NH_2-MIL-125(Ti) are 0.55 and 3.36 eV, respectively. The potential of the conduction band (CB) edge can be calculated from the VB and E_g values resulting in −1.51 and 0.72 eV for $CuGaS_2$ and NH_2-MIL-125(Ti), respectively.

Based on the above-discussed results, Fig. 9 illustrates the potential charge transfer mechanism for the photocatalytic H_2 generation of the CGS@MIL(Ti) photocatalyst. The proposed pathway of the photoprocess was based on the literature data [66–68] and the analysis of intermediate products in the post-irradiated electrolyte using the GC-MS technique (Fig. 7d). NH_2-MIL-125(Ti) is an n-type semiconductor with its Fermi energy level located close to the CB [48], while $CuGaS_2$ is a p-type semiconductor with its Fermi level near the VB [68]. When NH_2-MIL-125(Ti) contacts with $CuGaS_2$, the Fermi levels of NH_2-MIL-125(Ti) and $CuGaS_2$ tend to rise and descend, respectively. This establishes an equilibrium state and generates an inner electric field at the interface (see Fig. 9).

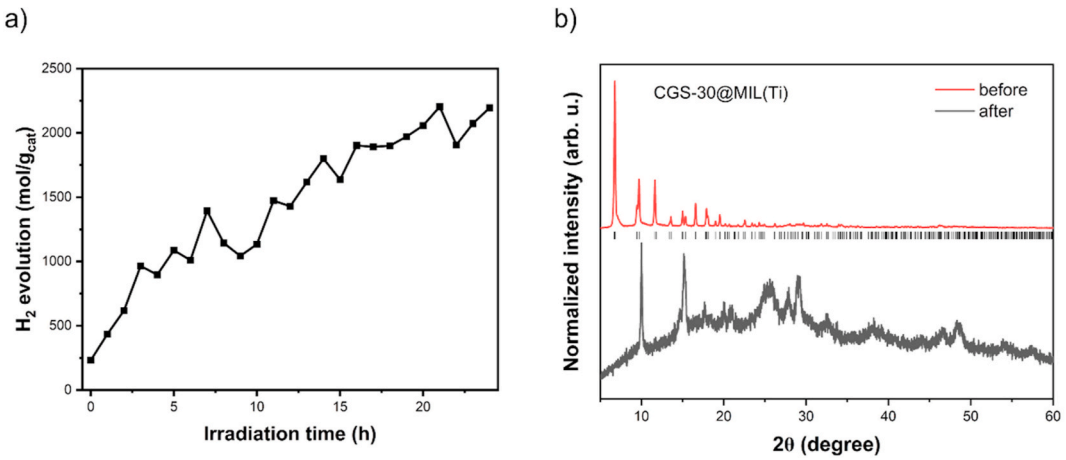

Fig. 8. a) Long-term stability of the CGS-30@MIL(Ti) sample, b) XRD patterns of the CGS-30@MIL(Ti) sample before and after 24 h of UV–Vis irradiation.

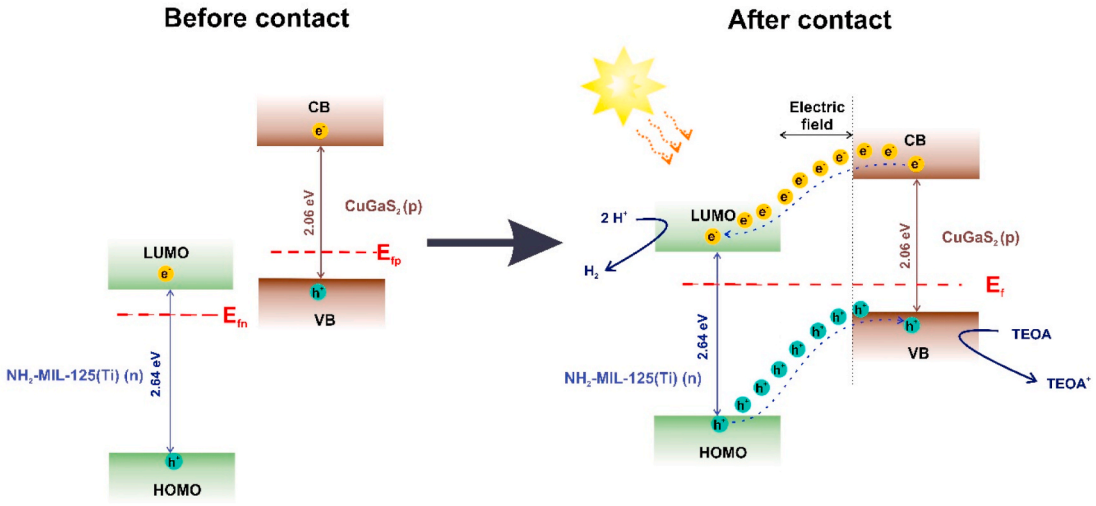

Fig. 9. Schematic diagram of (a) the band energy of NH_2-MIL-125(Ti) and $CuGaS_2$ before (a) and after (b) contact and the proposed charge transfer and separation process of $CuGaS_2$@NH_2-MIL-125(Ti) under UV–Vis irradiation.

Under UV–Vis irradiation, NH_2-MIL-125(Ti) can be easily excited, producing electrons and holes. The excited electrons in the CB of p-type $CuGaS_2$ move to LUMO of the n-type MOF, while the holes migrate from HOMO of NH_2-MIL-125(Ti) to the VB of $CuGaS_2$. This process effectively separates the photogenerated charge pairs, thereby enhancing the efficiency of the photocatalytic H_2 evolution system compared to individual compounds NH_2-MIL-125(Ti) and $CuGaS_2$. The electrons located in the LUMO of NH_2-MIL-125(Ti) reduce protons from water molecules, producing hydrogen as the desired product of the reaction. Meanwhile, TEOA prevents the oxidative action of holes in the VB of $CuGaS_2$. The VB of $CuGaS_2$ participates in the oxidation of TEAO (E_{ox} = 0.57–0.82 V vs. SCE) [69], leading to the formation of acetaldehyde, as confirmed by the GC-MS technique (see Fig. 7d).

4. Conclusions

In summary, a facial two-step synthesis method was used to prepare $CuGaS_2$@NH_2-MIL-125(Ti) nanocomposite. The introduction of chalcogenide during the solvothermal synthesis of MOF leads to the preservation of the morphology of both individual components, within the nanocomposite structure. As demonstrated, the CGS@MIL(Ti) material consisted of octahedral NH_2-MIL-125(Ti) interspersed with flat hexagonal plates of $CuGaS_2$. This observation underscores the successful integration of the two materials without compromising their intrinsic properties.

The photocatalytic H_2 production experiments demonstrated that pristine NH_2-MIL-125(Ti) and $CuGaS_2$ exhibited poor performance. However, when these components were combined, the photoactivity of $CuGaS_2$@NH_2-MIL-125(Ti) nanocomposite improved significantly. This enhancement is attributed to efficient charge separation and reduced recombination of photogenerated electron-hole pairs, resulting in superior photocatalytic activity compared to pristine NH_2-MIL-125(Ti) and $CuGaS_2$ components. We identified the optimal $CuGaS_2$ content to be 30 wt%, which resulted in the highest H_2 production efficiency of 965.1 μmol/g_{cat}. The calculated AQE of 9.07% at a wavelength of 380 nm further confirms the high photocatalytic efficiency of the $CuGaS_2$@NH_2-MIL-125(Ti) nanocomposite. However, the main issue of the proposed nanocomposite is its long-term stability, specifically concerning the NH_2-MIL-125(Ti) component, while $CuGaS_2$ remained prominent. It is suggested that the photogenerated electrons with the highest reducing potential reside within the conduction band (CB) of $CuGaS_2$. These electrons, due to their elevated potential, are hypothesized to potentially initiate the degradation of the MOF component present within the composite.

This research is a promising direction for future research in the field of photocatalytic hydrogen generation. Specifically, the utilization of $CuGaS_2$ chalcogenide as a reactant in solvothermal reactions holds potential for the development of efficient I-III-VI2 compound-MOF nanocomposites. Further investigations should focus on exploring different synthesis methods and optimizing nanocomposite compositions to enhance photocatalytic performance and stability even further.

CRediT authorship contribution statement

Anna Pancielejko: Writing – review & editing, Writing – original draft, Visualization, Validation, Methodology, Investigation, Data curation, Conceptualization. **Hanna Głowienke:** Writing – review & editing, Writing – original draft, Investigation. **Magdalena Miodyńska:** Writing – review & editing, Writing – original draft, Validation, Methodology, Investigation. **Anna Gołąbiewska:** Writing – original draft, Methodology. **Tomasz Klimczuk:** Investigation. **Mirosław Krawczyk:** Writing – original draft, Methodology, Investigation. **Krzysztof Matus:** Investigation. **Adriana Zaleska-Medynska:** Writing – review & editing, Supervision, Project administration, Funding acquisition, Conceptualization.

Declaration of competing interest

The authors declare that they have no known competing financial interests or personal relationships that could have appeared to influence the work reported in this paper.

Acknowledgment

This work has received financial support from the National Center for Research and Development. The project “Pioneering hybrid materials for CO_2 photoconversion” (acronym HotHybrids) No.: NOR/SGS/HotHybrids/0130/2020-00 is financed by the Financial Mechanism of the European Economic Area (EEA) and the Norwegian Financial Mechanism 2014–2021.

Appendix A. Supplementary data

Supplementary data to this article can be found online at https://doi.org/10.1016/j.ijhydene.2024.06.416.

References

[1] Safaei M, Foroughi MM, Ebrahimpoor N, Jahani S, Omidi A, Khatami M. A review on metal-organic frameworks: synthesis and applications. TrAC, Trends Anal Chem 2019;118:401–25. https://doi.org/10.1016/j.trac.2019.06.007.

[2] Li Y, Xu H, Ouyang S, Ye J. Metal-organic frameworks for photocatalysis. Phys Chem Chem Phys 2016;18:7563–72. https://doi.org/10.1039/c5cp05885f.

[3] Wang Q, Astruc D. State of the art and prospects in metal-organic framework (MOF)-Based and MOF-derived nanocatalysis. Chem Rev 2020;120:1438–511. https://doi.org/10.1021/acs.chemrev.9b00223.

[4] Kobielska PA, Howarth AJ, Farha OK, Nayak S. Metal–organic frameworks for heavy metal removal from water. Coord Chem Rev 2018;358:92–107. https://doi.org/10.1016/j.ccr.2017.12.010.

[5] Hu Z, Deibert BJ, Li J. Luminescent metal-organic frameworks for chemical sensing and explosive detection. Chem Soc Rev 2014;43:5815–40. https://doi.org/10.1039/c4cs00010b.

[6] Li JR, Kuppler RJ, Zhou HC. Selective gas adsorption and separation in metal-organic frameworks. Chem Soc Rev 2009;38:1477–504. https://doi.org/10.1039/b802426j.

[7] Murray LJ, Dinc M, Long JR. Hydrogen storage in metal-organic frameworks. Chem Soc Rev 2009;38:1294–314. https://doi.org/10.1039/b802256a.

[8] Reddy CV, Reddy KR, Harish VVN, Shim J, Shankar MV, Shetti NP, et al. Metal-organic frameworks (MOFs)-based efficient heterogeneous photocatalysts: synthesis, properties and its applications in photocatalytic hydrogen generation, CO2 reduction and photodegradation of organic dyes. Int J Hydrogen Energy 2020;45:7656–79. https://doi.org/10.1016/j.ijhydene.2019.02.144.

[9] Reddy DA, Kim Y, Gopannagari M, Kumar DP, Kim TK. Recent advances in metal-organic framework-based photocatalysts for hydrogen production. Sustain Energy Fuels 2021;5:1597–618. https://doi.org/10.1039/c9se00749k.

[10] Xiao JD, Jiang HL. Metal-organic frameworks for photocatalysis and photothermal catalysis. Acc Chem Res 2019;52:356–66. https://doi.org/10.1021/acs.accounts.8b00521.

[11] Liu S, Zhang C, Sun Y, Chen Q, He L, Zhang K, et al. Design of metal-organic framework-based photocatalysts for hydrogen generation. Coord Chem Rev 2020;413. https://doi.org/10.1016/j.ccr.2020.213266.

[12] Hayat A, Rauf S, Al Awan B, El Jery A, Melhi S, Amin MA, et al. Recent advance in MOFs and MOF-based composites: synthesis, properties, and applications. Mater Today Energy 2024;41:101542.

[13] Tahir M, Ajiwokewu B, Bankole AA, Ismail O, Al-Amodi H, Kumar N. MOF based composites with engineering aspects and morphological developments for photocatalytic CO2 reduction and hydrogen production: a comprehensive review. J Environ Chem Eng 2023;11.

[14] Do HH, Nguyen THC, Nguyen T Van, Xia C, Nguyen DLT, Raizada P, et al. Metal-organic-framework based catalyst for hydrogen production: progress and perspectives. Int J Hydrogen Energy 2022;47:37552–68. https://doi.org/10.1016/j.ijhydene.2022.01.080.

[15] Kavun V, Uslamin E, van der Linden B, Canossa S, Goryachev A, Bos EE, et al. Promoting photocatalytic activity of NH2-MIL-125(Ti) for H2 evolution reaction through creation of TiIII- and CoI-based proton reduction sites. ACS Appl Mater Interfaces 2023. https://doi.org/10.1021/acsami.3c15490.

[16] Horiuchi Y, Toyao T, Saito M, Mochizuki K, Iwata M, Higashimura H, et al. Visible-light-promoted photocatalytic hydrogen production by using an amino-functionalized Ti(IV) metal-organic framework. J Phys Chem C 2012;116:20848–53. https://doi.org/10.1021/jp3046005.

[17] Sun M, Yu F, Wang J, Wang Y, Jing X, Duan C. d-NH2-MIL-125 doped with Cu NPs for light-driven hydrogen evolution. Chem Commun 2023;59:8456–9. https://doi.org/10.1039/d3cc01770b.

[18] Baluk MA, Mazierski P, Pieczyńska A, Nikiforow K, Trykowski G, Klimczuk T, et al. MOF/TiO2 erythrocyte-like heterostructures decorated by noble metals for use in hydrogen photogeneration and pollutant photodegradation. Catal Sci Technol 2023;13:5033–47. https://doi.org/10.1039/d3cy00531c.

[19] Zhou Y, Zhao X, Liang Q, Zhou M, Li X, Xu S, et al. In situ growth of CdIn2S4 on NH2-MIL-125 as efficient photocatalysts for H2 production under visible-light irradiation. J Phys Chem Solid 2023;173. https://doi.org/10.1016/j.jpcs.2022.111096.

[20] Ikreedeegh RR, Tasleem S, Hossen MA. Facile fabrication of binary g-C3N4/NH2-MIL-125(Ti) MOF nanocomposite with Z-scheme heterojunction for efficient photocatalytic H2 production and CO2 reduction under visible light. Fuel 2024;360. https://doi.org/10.1016/j.fuel.2023.130561.

[21] Li H, Liu X, Feng H, Zhao J, Lu P, Fu M, et al. NH2-MIL-125(Ti) with transient metal centers: via novel electron transfer routes for enhancing photocatalytic NO removal and H2evolution. Catal Sci Technol 2021;11:6225–33. https://doi.org/10.1039/d1cy01008e.

[22] Jiang D, Xu P, Wang H, Zeng G, Huang D, Chen M, et al. Strategies to improve metal organic frameworks photocatalyst's performance for degradation of organic pollutants. Coord Chem Rev 2018;376:449–66. https://doi.org/10.1016/j.ccr.2018.08.005.

[23] Xu J, Gao J, Wang C, Yang Y, Wang L. NH2-MIL-125(Ti)/graphitic carbon nitride heterostructure decorated with NiPd co-catalysts for efficient photocatalytic hydrogen production. Appl Catal, B 2017;219:101–8. https://doi.org/10.1016/j.apcatb.2017.07.046.

[24] Nivetha R, Gothandapani K, Raghavan V, Jacob G, Sellapan R, Kannan AM, et al. NH2-MIL-125(Ti) doped CdS/Graphene composite as electro and photo catalyst in basic medium under light irradiation. Environ Res 2021;200. https://doi.org/10.1016/j.envres.2021.111719.

[25] Li S, Tang X, Zang Z, Yao Y, Yao Z, Zhong H, et al. I-III-VI chalcogenide semiconductor nanocrystals: synthesis, properties, and applications. Cuihua Xuebao/Chinese Journal of Catalysis 2018;39:590–605. https://doi.org/10.1016/S1872-2067(18)63052-9.

[26] Matussin SN, Rahman A, Khan MM. Role of anions in the synthesis and crystal growth of selected semiconductors. Front Chem 2022;10. https://doi.org/10.3389/fchem.2022.881518.

[27] Khan MM, Rahman A. Chalcogenides and chalcogenide-based heterostructures as photocatalysts for water splitting. Catalysts 2022;12. https://doi.org/10.3390/catal12111338.

[28] Meng X, Zuo G, Zong P, Pang H, Ren J, Zeng X, et al. A rapidly room-temperature-synthesized Cd/ZnS:Cu nanocrystal photocatalyst for highly efficient solar-light-powered CO2 reduction. Appl Catal, B 2018;237:68–73. https://doi.org/10.1016/j.apcatb.2018.05.066.

[29] Wang Y, Chen J, Liu L, Xi X, Li Y, Geng Z, et al. Novel metal doped carbon quantum dots/CdS composites for efficient photocatalytic hydrogen evolution. Nanoscale 2019;11:1618–25. https://doi.org/10.1039/c8nr05807e.

[30] Pang H, Meng X, Song H, Zhou W, Yang G, Zhang H, et al. Probing the role of nickle dopant in aqueous colloidal ZnS nanocrystals for efficient solar-driven Nickel reduction. Appl Catal, B 2019;244:1013–20. https://doi.org/10.1016/j.apcatb.2018.12.010.

[31] Kaga H, Tsutsui Y, Nagane A, Iwase A, Kudo A. An effect of Ag(i)-substitution at Cu sites in CuGaS2 on photocatalytic and photoelectrochemical properties for solar hydrogen evolution. J Mater Chem A Mater 2015;3:21815–23. https://doi.org/10.1039/c5ta04756k.

[32] Xu W, Xie Z, Han W, Zhang K, Guo D, Chang K. Rational design of interfacial energy level matching for CuGaS2 based photocatalysts over hydrogen evolution reaction. Int J Hydrogen Energy 2022;47:11853–62. https://doi.org/10.1016/j.ijhydene.2022.01.209.

[33] Kaga H, Tsutsui Y, Nagane A, Iwase A, Kudo A. An effect of Ag(i)-substitution at Cu sites in CuGaS2 on photocatalytic and photoelectrochemical properties for solar hydrogen evolution. J Mater Chem A Mater 2015;3:21815–23. https://doi.org/10.1039/c5ta04756k.

[34] Caudillo-Flores U, Kubacka A, Berestok T, Zhang T, Llorca J, Arbiol J, et al. Hydrogen photogeneration using ternary CuGaS2-TiO2-Pt nanocomposites. Int J Hydrogen Energy 2020;45:1510–20. https://doi.org/10.1016/j.ijhydene.2019.11.019.

[35] Son N, Heo JN, Youn YS, Kim Y, Do JY, Kang M. Enhancement of hydrogen productions by accelerating electron-transfers of sulfur defects in the CuS@CuGaS2 heterojunction photocatalysts. Catalysts 2019;9. https://doi.org/10.3390/catal9010041.

[36] Chang SH, Chiu BC, Gao TL, Jheng S Lou, Tuan HY. Selective synthesis of copper gallium sulfide (CuGaS2) nanostructures of different sizes, crystal phases, and morphologies. CrystEngComm 2014;16:3323–30. https://doi.org/10.1039/c3ce42530d.

[37] Adhikari S Das, Dutta A, Prusty G, Sahu P, Pradhan N. Symmetry break and seeded 2D anisotropic growth in ternary CuGaS2 nanocrystals. Chem Mater 2017;29:5384–93. https://doi.org/10.1021/acs.chemmater.7b01775.

[38] Marquardt J, Gurieva G, Stephan-Scherb C, Schorr S. The effect of copper vacancies on the anion position of chalcopyrite type CuGaS2. Physica Status Solidi (A) Applications and Materials Science 2019;216. https://doi.org/10.1002/pssa.201800882.

[39] Zhao M, Huang F, Lin H, Zhou J, Xu J, Wu Q, et al. CuGaS2-ZnS p-n nanoheterostructures: a promising visible light photo-catalyst for water-splitting hydrogen production. Nanoscale 2016;8:16670–6. https://doi.org/10.1039/c6nr05002f.

[40] Liu A, Yu C, Lin J, Sun G, Xu G, Huang Y, et al. Construction of CuInS2@ZIF-8 nanocomposites with enhanced photocatalytic activity and durability. Mater Res Bull 2019;112:147–53. https://doi.org/10.1016/j.materresbull.2018.12.020.

[41] Nguyen HVT, Nguyen MB, Doan HV, Pham XN. A green synthesis of CuInS2/MIL-101(Cr) nanocomposite with efficient visible light induced photocatalytic activity. Mater Res Express 2023;10. https://doi.org/10.1088/2053-1591/acf18f.

[42] Pham XN, Vu VT, Nguyen HVT, Nguyen TTB, Doan HV. Designing a novel heterostructure AgInS2@MIL-101(Cr) photocatalyst from PET plastic waste for tetracycline degradation. Nanoscale Adv 2022;4:3600–8. https://doi.org/10.1039/d2na00371f.

[43] Liu H, Zhang J, Ao D. Construction of heterostructured ZnIn2S4@NH2-MIL-125 (Ti) nanocomposites for visible-light-driven H2 production. Appl Catal, B 2018;221:433–42. https://doi.org/10.1016/j.apcatb.2017.09.043.

[44] Jin P, Wang L, Ma X, Lian R, Huang J, She H, et al. Construction of hierarchical ZnIn2S4@PCN-224 heterojunction for boosting photocatalytic performance in hydrogen production and degradation of tetracycline hydrochloride. Appl Catal, B 2021;284. https://doi.org/10.1016/j.apcatb.2020.119762.

[45] Yao H, Sui G, Li J, Guo D, Wang J, Yue Y, et al. Ni-MOF-74-derived ZnIn2S4/P-Ni-MOF-74 Z-scheme heterojunctions for highly efficient photocatalytic hydrogen evolution under visible light irradiation. J Mol Struct 2023;1284. https://doi.org/10.1016/j.molstruc.2023.135398.

[46] Deng EZ, Fan YZ, Wang HP, Li Y, Peng C, Liu J. Engineering a Z-scheme heterostructure on ZnIn2S4@NH2-MIL-125 composites for boosting the

photocatalytic performance. Inorg Chem 2024;63:1449–61. https://doi.org/10.1021/acs.inorgchem.3c03968.
[47] Ye JQ, Dai YZ, Xu SY, Wang PX, Sun ZH, Qian JF, et al. Synergistic enhancement of photocatalytic H2 evolution over NH2-MIL-125 modified with dual cocatalyst. Inorg Chem 2023. https://doi.org/10.1021/acs.inorgchem.3c03502.
[48] Sk S, Mondal I, Mahata A, Abraham BM, Nayak C, Bhattacharyya D, et al. Function of defects in NH2-MIL-125@PANI@Co3O4Photocatalyst for efficient hydrogen evolution. ACS Appl Energy Mater 2022;5:12324–35. https://doi.org/10.1021/acsaem.2c01899.
[49] Liu Z, Hao Q, Tang R, Wang L, Tang K. Facile one-pot synthesis of polytypic CuGaS 2 nanoplates. 2013.
[50] Nevárez Martínez MC, Cavdar O, Haliński ŁP, Miodyńska M, Parnicka P, Bajorowicz B, et al. Hydrogen detection during photocatalytic water splitting: a tutorial. Int J Hydrogen Energy 2022;47:15783–8. https://doi.org/10.1016/j.ijhydene.2022.03.050.
[51] Chakraborty S, Das R, Riyaz M, Das K, Singh AK, Bagchi D, et al. Wurtzite CuGaS2 with an in-situ-formed CuO layer photocatalyzes CO2 conversion to ethylene with high selectivity. Angew Chem Int Ed 2023;62. https://doi.org/10.1002/anie.202216613.
[52] Liu L, Du S, Xiao Y, Guo X, Jin S, Shao G, et al. Saturated Ti-coordinated {001} facets-dependent photocatalytic water reduction over NH2-MIL-125(Ti) sheets: observation and unraveling of facets effect. Appl Catal, B 2023;338:123094. https://doi.org/10.1016/j.apcatb.2023.123094.
[53] Zhang R, Liu Y, Wang C, Li Y, Zhu Q, Zhang S, et al. Constructing bifunctional TiO2 from NH2-MIL-125(Ti) for excellent photocatalytic tetracycline degradation. J Alloys Compd 2023;965:171396. https://doi.org/10.1016/j.jallcom.2023.171396.
[54] Moulder JF, Stickle W, Sobol Peter E, Bomben Kenneth D. Handbook of X-ray photoelectron spectroscopy. Physical Electronics Inc.; 1996.
[55] Naukin CJPA V., Kraut-Vass A, Gaarenstroom W. NIST X-ray photoelectron spectroscopy database 20, Version 4.1: http://srdata.nist.gov/xps/n.d..
[56] Beamson G, Briggs D. High resolution XPS of organic polymers: the scienta ESCA300 database. John Willey and Sons Ltd; 1992.
[57] Biesinger MC. Advanced analysis of copper X-ray photoelectron spectra. Surf Interface Anal 2017;49:1325–34. https://doi.org/10.1002/sia.6239.
[58] Berestok T, Guardia P, Estradé S, Llorca J, Peiró F, Cabot A, et al. CuGaS2 and CuGaS2–ZnS porous layers from solution-processed nanocrystals. Nanomaterials 2018;8. https://doi.org/10.3390/nano8040220.
[59] Ao D, Zhang J, Liu H. Visible-light-driven photocatalytic degradation of pollutants over Cu-doped NH2-MIL-125(Ti). J Photochem Photobiol Chem 2018;364:524–33. https://doi.org/10.1016/j.jphotochem.2018.06.044.
[60] Fu Y, Sun L, Yang H, Xu L, Zhang F, Zhu W. Visible-light-induced aerobic photocatalytic oxidation of aromatic alcohols to aldehydes over Ni-doped NH2-MIL-125(Ti). Appl Catal, B 2016;187:212–7. https://doi.org/10.1016/j.apcatb.2016.01.038.
[61] Fu Y, Sun D, Chen Y, Huang R, Ding Z, Fu X, et al. An amine-functionalized titanium metal-organic framework photocatalyst with visible-light-induced activity for CO 2 reduction. Angew Chem Int Ed 2012;51:3364–7. https://doi.org/10.1002/anie.201108357.
[62] Isik M, Gullu HH, Coskun E, Gasanly NM. Optical band gap and dispersion of optical constants of Cu-Ga-S thin films. Optik 2019;186:147–54. https://doi.org/10.1016/j.ijleo.2019.04.035.
[63] Alonso MI, Wakita K, Pascual J, Garriga M, Yamamoto N. Optical functions and electronic structure of CuInSe2, CuGaSe2, CuInS2, and CuGaS2. Phys Rev B Condens Matter 2001;63. https://doi.org/10.1103/PhysRevB.63.075203.
[64] Shen Y, Zhu C, Chen B, Chen J, Fang Q, Wang J, et al. Novel photocatalytic performance of nanocage-like MIL-125-NH2induced by adsorption of phenolic pollutants. Environ Sci Nano 2020;7:1525–38. https://doi.org/10.1039/d0en00120a.
[65] Liu H, Zhang J, Ao D. Construction of heterostructured ZnIn2S4@NH2-MIL-125 (Ti) nanocomposites for visible-light-driven H2 production. Appl Catal, B 2018;221:433–42. https://doi.org/10.1016/j.apcatb.2017.09.043.
[66] Muelas-Ramos V, Sampaio MJ, Silva CG, Bedia J, Rodriguez JJ, Faria JL, et al. Degradation of diclofenac in water under LED irradiation using combined g-C3N4/NH2-MIL-125 photocatalysts. J Hazard Mater 2021;416. https://doi.org/10.1016/j.jhazmat.2021.126199.
[67] He S, Rong Q, Niu H, Cai Y. Platform for molecular-material dual regulation: a direct Z-scheme MOF/COF heterojunction with enhanced visible-light photocatalytic activity. Appl Catal, B 2019;247:49–56. https://doi.org/10.1016/j.apcatb.2019.01.078.
[68] Wu S, Pang H, Zhou W, Yang B, Meng X, Qiu X, et al. Stabilizing CuGaS2 by crystalline CdS through an interfacial Z-scheme charge transfer for enhanced photocatalytic CO2 reduction under visible light. Nanoscale 2020;12:8693–700. https://doi.org/10.1039/d0nr00483a.
[69] Pellegrin Y, Odobel F. Les donneurs d'électron sacrificiels pour la production de combustible solaire. Compt Rendus Chem 2017;20:283–95. https://doi.org/10.1016/j.crci.2015.11.026.